Research Article | Vol. 31, No. 23 / 6 Nov 2023 / Optics Express 37892
Optics EXPRESS

Silicon nitride TM-pass polarizer using inverse design

JULIAN L. PITA RUIZ,* FREDERIC NABKI, AND MICHAËL MÉNARD

Department of Electrical Engineering, École de Technologie Supérieure (ÉTS), Montreal, QC, H3C 1K3, Canada
julian-leonel.pita-ruiz@etsmtl.ca

Abstract: Integrated silicon nitride polarizers play a critical role in the design of complex integrated devices such as filters, switches, and large Mach-Zehnder interferometer networks. These devices require precise control of both polarizations on a single circuit. In addition, polarizers are essential to accurately characterize these devices, primarily due to the low efficiency and polarization extinction ratio (PER) of the surface coupling gratings used in CMOS-compatible silicon nitride platforms for test-specific optical I/O. In this article, we present the design and experimental performance of six prototypes of TE-reflector/TM-pass polarizers specifically optimized for the C-band. These prototypes resemble subwavelength gratings with several additional intricate aspects. In particular, the longer prototypes feature two distinct regions, one representing non-intuitive tapers and the other showcasing a more distinct subwavelength grating. We achieve a high TM transmission efficiency of −0.28 dB along with a PER of 18.2 dB. These results are obtained with a device occupying an area as low as 11 µm × 2 µm, setting a new performance benchmark for compact polarizers compatible with standard silicon nitride platforms.

1. Introduction

The strong demand for high-performance optical links, driven by the significant growth of Internet traffic in recent years [1,2], has prompted academia and industry to explore methods to increase their capacity [3–5]. Advanced modulation systems with coherent detection have been developed to improve spectral efficiency [6,7]. In addition, wavelength, space, and polarization multiplexing have been explored as means to increase transmission capacity, with polarization multiplexing having the potential to double it [8–11]. The integration of dual-polarization circuits is not only desirable for optical communications but it also plays a critical role in applications such as sensors and signal processors [12,13]. Key components that enable integrated circuits to operate with two polarizations include polarization splitters [14–16], polarization rotators [17–19], and polarizers [20–24]. Despite significant progress in silicon photonics, developing compact chips that can fully manage both the tranverse magnetic (TM) and transverse electric (TE) polarizations remains a challenge [25].

In recent years, various methods were proposed to design polarizers, including techniques relying on a single core layer, typically made of silicon, and others incorporating additional materials such as conductive oxides [26], graphene [27] or metals [28,29]. There are two main approaches to single-layer polarizers: material doping [30] and geometry-based designs [31]. The former tends to have high insertion loss and a more complex manufacturing process, thus this paper focuses on the latter. Geometry-based polarizers, particularly subwavelength grating (SWG), have received considerable attention. SWGs have a simple design and compact size, which allows for easy adjustment of the operational wavelengths by tuning the grating parameters [32,33]. For instance, Yufei *et al.* introduced a silicon TM-pass polarizer with an insertion loss of about 1 dB and a PER exceeding 15 dB over a broad wavelength range from 1300 nm to 1600 nm

#503124 https://doi.org/10.1364/OE.503124
Journal © 2023 Received 15 Aug 2023; revised 27 Sep 2023; accepted 17 Oct 2023; published 24 Oct 2023

Optics EXPRESS

[31]. Similarly, Xiaowei *et al.* demonstrated a compact silicon TM-pass polarizer having a size of 500 nm × 9 µm providing an insertion loss of 0.5 dB and a PER of 27 dB [32]. While significant progress has been made in silicon-based polarizers, there is still a lack of high-performance polarizers in widely used integrated photonic platforms based on silicon nitride. In this context, Kyu J. Lee *et al.* demonstrated a silicon nitride polarizer with a loss of 0.2 dB and a PER of 15 dB. This polarizer was built on a 464 nm SiN thin film with an etch depth of 362 nm and an air top-cladding [34].

In this article, we present six silicon nitride polarizers models designed using topological optimization. We explored different lengths and widths in the optimization space, ranging from 7 µm to 12 µm and from 0.85 µm to 3 µm, respectively. The devices were designed with a minimum feature and space size of 200 nm and a single and complete etch of the silicon nitride layer, facilitating their fabrication in commercial multi-project wafer (MPW) runs. One of the TM-pass polarizers has an area of 11 µm × 2 µm and exhibits an insertion loss of 0.28 dB and PER greater than 15 dB over the C-band. These polarizers enable the implementation of complex silicon nitride devices, such as wavelength division multiplexing (WDM) filters, switches, and Mach-Zehnder networks that operate with both polarizations.

2. Design

To ensure compatibility with standard CMOS manufacturing processes, we employed a silicon nitride-on-insulator (SNOI) wafer with a 400 nm silicon nitride layer for the design of all the couplers. Commercial software from Ansys Lumerical was used for the design process. Gradient-based 3D topology optimization was performed using the LumOpt API, while the Finite Difference Time Domain (FDTD) 3D module was used for verification simulations. An optimization region of 7 µm in length and 4 µm in width was initially defined, with the input and output waveguide widths set at 850 nm. The goal defined by the objective function was to maximize the coupling efficiency of the fundamental mode TM into the output and the reflection of the fundamental TE mode towards the input, using 5 wavelengths distributed over the entire C- and L-bands.

Figure 1(a) illustrates the optimization trajectory, showing the convergence of the coupling efficiency for both the transmitted TM mode and the reflected TE mode to values of −0.38 dB and −0.48 dB (averaged over all wavelengths), respectively. After iteration 25, the objective function shows minimal changes, although the geometry of the device undergoes significant changes during these iterations due to the binarization process of the refractive index. Figure 1(a) also includes two insets showing the refractive index distribution of the polarizer. The first inset corresponds to iteration 2, while the second inset represents iteration 131, which is near the end of the binarization process. It is worth noting that there is no abrupt drop in the objective function due to the imposition of manufacturing parameters. It should also be mentioned that several initial conditions were tested, including starting with an optimization region entirely made of silicon nitride, silicon dioxide, or a fictitious material with a refractive index of 1.75, and matrices with random values between the refractive index of silicon and the one of silicon dioxide. For these particular devices, starting with an optimization region simulating silica yielded the best initial conditions. Figure 1(b) shows a schematic of the polarizer illustrating its principle of operation.

After each optimization, a more accurate FDTD 3D verification simulation was performed using a finer mesh than the one used during optimization. This is because, during the optimization process, a coarser mesh providing a trade-off between simulation time and accuracy was used. Typically, the optimization process consists of approximately 120 iterations, with each iteration taking about 2 to 4 minutes on a computer with 64 GB of RAM and an Intel Core i9-12900 processor. Although an optimization region width of up to 4 µm was tested, a width of 2 µm was ultimately selected. This was based on the fact that removing the silicon nitride index outside the

Optics EXPRESS

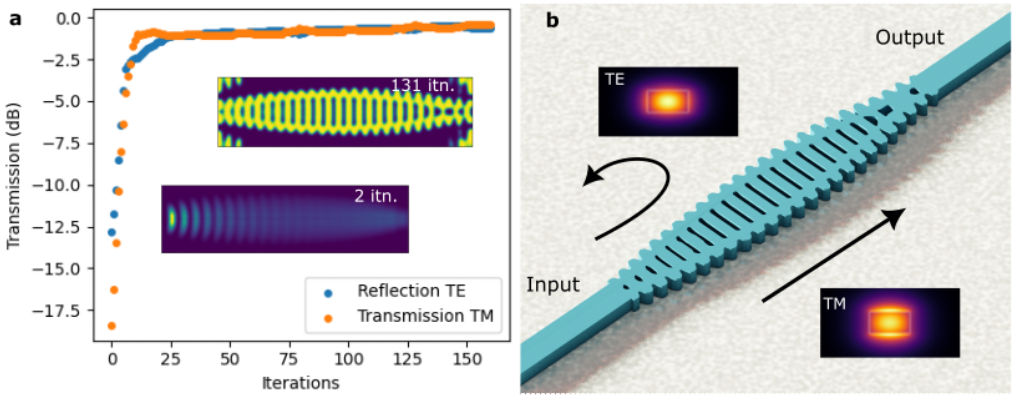

Fig. 1. Optimization process of the polarizers. a) Optimization trajectory of the 7-μm length polarizer. The orange dots represent the coupling efficiency of the transmitted fundamental TM mode, while the blue dots represent the reflected fundamental TE mode. The insets illustrate the distribution of the refractive index at iterations 2 and 131, respectively. b) Schematic showing the operating principle of the polarizer.

2 μm region did not significantly affect the performance of the polarizer in terms of transmission efficiency or PER. In addition, it significantly reduced the time required for the optimization process.

Figure 2 shows the simulated performance of the six optimized devices. Figure 2(a) and (b) show the electric field magnitude of the TE and TM modes and the refractive index contour for the 9 and 12-μm-long polarizers, respectively. It is worth noting that while the geometries of the prototypes resemble SWGs, these incorporate more complex characteristics that enable compact devices without compromising performance. In the larger designs, two distinct regions emerge, a non-intuitive taper region near the waveguides and another region that mimics a conventional SWG, as depicted in Fig. 2(a) corresponding to the 12 μm long prototype. In contrast, for the shorter devices, these two regions are less distinguishable, as shown in Fig. 2(a) for the 9 μm prototype. Figure 2(c) illustrates the evolution of the effective index for the fundamental TE and TM modes at a wavelength of 1550 nm as a function of position along the 12 μm long polarizer. This visualization confirms that the device behaves similarly to a SWG with a period of 480 nm and a duty cycle of 0.76. Furthermore, it is evident that the TE mode experiences a stronger index contrast compared to the TM mode. Figure 2(d) shows two distinct trends because the initial optimizations, which were done for the shorter devices that are between 7 and 9 μm long, were performed over the C- and L-bands, resulting in a low PER. Consequently, the optimization wavelengths were narrowed down to only the C-band for the longer devices, leading to an increase in PER. For the three shorter devices, it can be observed that they all exhibit a maximum TM transmission efficiency close to −0.2 dB. In addition, these devices exhibit a very wide 3-dB bandwidth for the TM mode transmission efficiency, which extends over the entire 100 nm simulation band. However, the PER is relatively low, ranging from 8.4 to 10.4 dB for wavelengths around 1565 nm for all three devices. Conversely, at lower wavelengths, the PER reaches values as high as 20.2 dB for the 9-μm-long polarizer. On the other hand, the 10 to 12-μm polarizers have a PER that ranges from 14 to 20 dB over the entire C-band. It should be noted, however, that the TM coupling efficiency decreases, especially for wavelengths below 1550 nm. Among these devices, the 12-μm polarizer shows the best simulation results with an insertion loss of 0.36 dB and a PER of approximately 20 dB over the entire C-band.

Optics EXPRESS

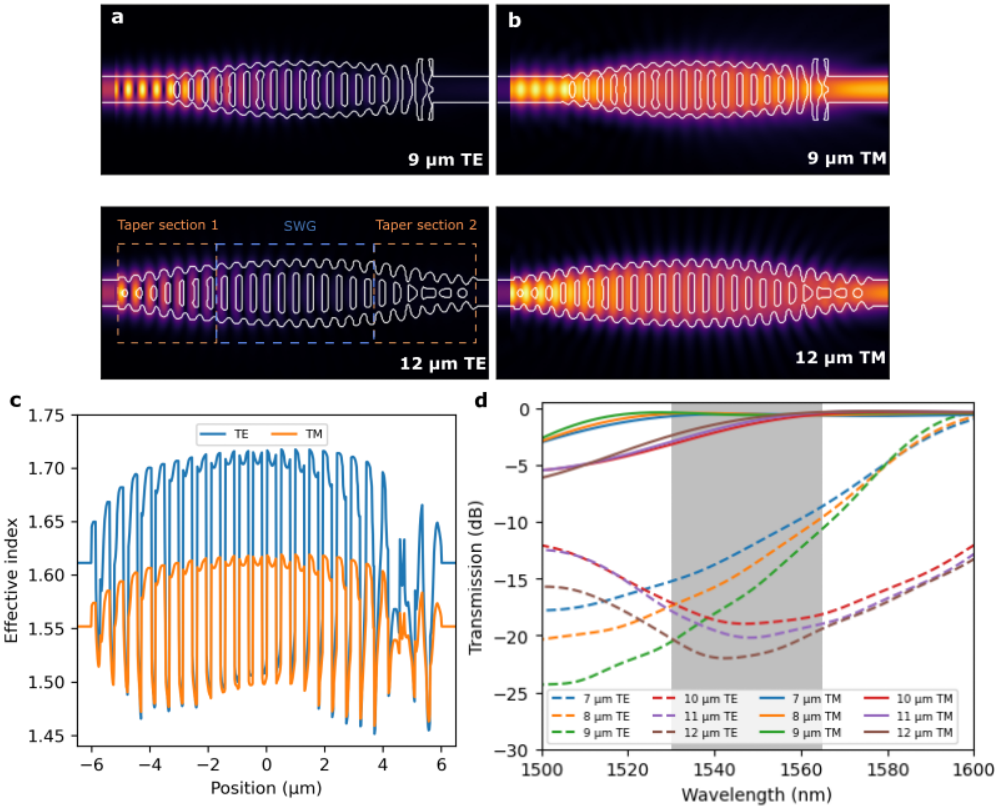

Fig. 2. Simulations of the polarizers. a) and b) Electric field of the reflected TE mode and the transmitted TM mode for the 9 and 12-µm long devices, respectively. c) Evolution of the effective index for the fundamental TE and TM modes at a wavelength of 1550 nm as a function of position for the 12 µm long polarizer. d) Coupling efficiency for both the TE (solid lines) and TM (dashed lines) polarization for all devices.

3. Results

The platform selected for implementing the prototypes was a SNOI wafer consisting of a 400 nm thick device layer, a 4.5 µm buried silica layer, and a 3 µm silica top cladding layer. The polarizers were fabricated using electron-beam lithography (EBL) and full-etch patterning by applied nanotools (ANT). A plasma-enhanced chemical vapor deposition process was used to deposit the top silicon dioxide cladding. Although the EBL process is capable of achieving a minimum feature size and spacing of 120 nm, a larger minimum feature size and spacing of 200 nm was chosen to ensure repeatability and compatibility with large-scale CMOS fabrication platforms. The scanning electron microscopy (SEM) images in Figs. 3(a) and (b) show the fabricated 11 and 12-µm polarizers along with their respective input and output waveguides. The waveguides have a rectangular cross-section of 850 nm × 400 nm. A comparison of the SEM image of the 12-µm long device presented in Fig. 3(b) with the schematic provided in Fig. 2(a) shows the high degree of fidelity of the fabricated devices, which retained all the key design features.

The polarizers were characterized by connecting the input and output waveguides to focused grating couplers designed for a single-mode fiber supporting both polarizations. They were laid out in a loopback (u-shape) configuration with Euler bends having a radius of 100 µm to

Optics EXPRESS

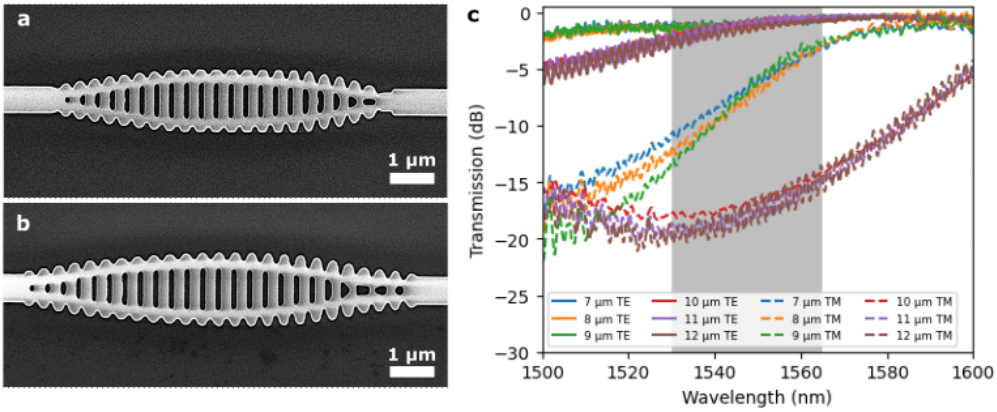

Fig. 3. Fabricated devices and their performance. (a) SEM image of the 11-µm-long polarizer. (b) SEM image of the 12-µm-long polarizer. (c) TM and TE transmission efficiencies of the six polarizers. The solid line indicates the TM transmission efficiency whereas the dotted line represents the TE transmission efficiency.

minimize curvature induced losses. The characterization setup consisted of an EXFO tunable laser, a polarization-maintaining (PM) fiber connected directly to a fiber array equipped with PM fibers for coupling to the TE mode on-chip. Additionally, a slow-to-fast axis fiber adapter was connected between the PM fiber and the fiber array to couple to the TM mode. The 8-fiber array was aligned to the loopback gratings at an angle of 31° for coupling to the TE mode, and of 28° for coupling to the TM mode. The power at the output of the fiber array was measured using an EXFO CTP440 detector. To normalize the results, the linear and coupling losses were calculated for the loopbacks without polarizers that were in close proximity to the prototypes. These calibration procedures yielded a transmission loss through the loopback structures without polarizers of 12.1 dB for the TE mode and of 15.7 dB for the TM mode, including the coupling losses of the two gratings and the propagation loss.

The results from the characterization of the transmission spectrum of the polarizers are shown in Fig. 3(c), where the solid lines represent the transmission of the TM mode and the dashed lines represent the transmission of the TE mode. The results obtained are in good agreement with the simulations, and show the same two trends described above. However, there is a noticeable shift of about 18 nm towards the lower wavelengths in all of the curves, which can be attributed to variations in the fabrication process. For devices larger than 9 µm, the TE transmission is below −13.5 dB, with the 12-µm-long device reaching a minimum transmission of −20.4 dB. On the other hand, devices shorter than 10 µm show a TE mode transmission efficiency of approximately −3 dB for wavelengths close to 1565 nm, whereas the 9-µm-long device shows a minimum transmission of −13.9 dB. Regarding the TM transmission, all devices exceed a minimum efficiency of −0.7 dB in the C-band, with the 10-µm-long polarizer achieving an efficiency of −0.23 dB at 1565.7 nm.

Figure 4 shows the maximum PER within the C-band. It can be observed that the PER increases with the size of the polarizer, reaching a value of 18.2 dB for the 11-µm-long device. However, for the 12-µm-long polarizer, the PER is slightly lower. It can be concluded that the 11-µm-long polarizer provides the best experimental performance among the fabricated prototypes. It has a TM transmission efficiency of −0.28 dB, a 3-dB bandwidth for the transmission of the TM mode of over 80 nm, and a PER that is greater than 14.3 dB throughout the C-band.

Table 1 compares the performance of the best device presented in this work with other single-layer polarizers reported in the literature. The comparison shows that silicon polarizers

Optics EXPRESS

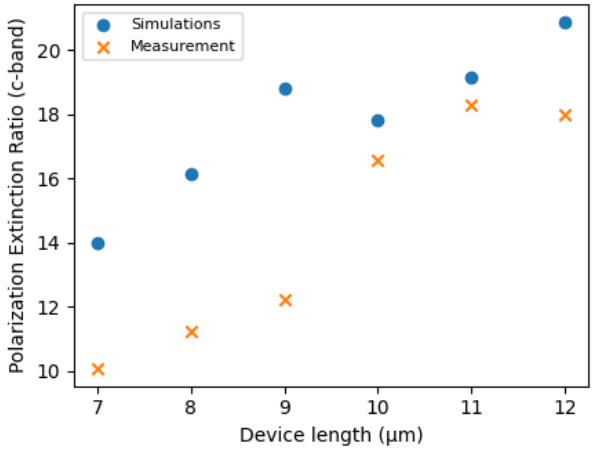

Fig. 4. Maximum simulated and measured PER across the C-band. The dot indicates simulations and the cross indicates measurements.

have a higher PER compared to silicon nitride polarizers. Nevertheless, both the polarizers from Kyu *et al.* [34] and the 11-μm-long polarizer from this work have lower insertion losses than the silicon polarizers. However, it is important to note that the device of Kyu *et al.* was built without a top cladding, and included an intermediate etching step [34]. Additionally, the 11-μm-long polarizer achieves a larger PER and bandwidth compared to the other silicon nitride polarizer, making it a promising design thanks to its simpler fabrication process.

Table 1. Comparison of various reported single-layer TM-pass polarizers

Ref	IL	Max. PER (dB)	Device length (μm)	Material	Operational band
Yufei et al. [21]	<1	38	13.6	Silicon	S-, C-, and L-bands
Xiaowei et al. [32]	0.5	27	9	Silicon	C-band
Kyu et al. [34]	0.2	15	-	Silicon Nitride	1580-1589 nm
This work	0.2	18.2	11	Silicon Nitride	C-band

4. Conclusion

We presented the design and experimental characterization of six silicon nitride TM-pass polarizers optimized for the C-band. These polarizers were designed using a commercial inverse design method and are compatible with standard silicon nitride platforms. The 11 μm × 2 μm polarizer has a maximum TM transmission efficiency of −0.28 dB and a PER that is greater than 15 dB over the entire C-band. The compact dimensions and performance of this polarizer make it ideal for seamless integration into complex integrated photonics devices that must process each polarization separately.

Funding. PRIMA Quebec (R16-46-002 PSO); Natural Sciences and Engineering Research Council of Canada (CRDPJ 530551 - 18).

Acknowledgments. The authors express their gratitude to AEPONYX Inc. for their generous support and for providing access to their test facilities. Additionally, they would like to thank CMC Microsystems for their assistance with the fabrication of the devices.

Disclosures. JLP: AEPONYX (F), FN: AEPONYX (F,P), MM: AEPONYX (F,P)

Data availability. Data underlying the results presented in this paper are not publicly available at this time but may be obtained from the authors upon reasonable request.

Optics EXPRESS

References

1. "Internet Traffic Statistics And Trends in 2023 • GITNUX," (2023). Section: Statistics.
2. P. J. Winzer, D. T. Neilson, and A. R. Chraplyvy, "Fiber-optic transmission and networking: the previous 20 and the next 20 years," Opt. Express **26**(18), 24190–24239 (2018).
3. Y. Shi, Y. Zhang, and Y. Wan, *et al.*, "Silicon photonics for high-capacity data communications," Photonics Res. **10**(9), A106–A134 (2022).
4. H. Yu, D. Patel, and W. Liu, *et al.*, "800 gbps fully integrated silicon photonics transmitter for data center applications," in *Optical Fiber Communication Conference*, (Optica Publishing Group, 2022), pp. M2D–7.
5. X. Zhou, R. Urata, and H. Liu, "Beyond 1 tb/s intra-data center interconnect technology: Im-dd or coherent?" J. Lightwave Technol. **38**(2), 475–484 (2020).
6. M. Kong, X. Li, and J. Zhang, *et al.*, "High spectral efficiency 400 gb/s transmission by different modulation formats and advanced dsp," J. Lightwave Technol. **37**(20), 5317–5325 (2019).
7. E. Ip, A. P. T. Lau, and D. J. Barros, *et al.*, "Coherent detection in optical fiber systems," Opt. Express **16**(2), 753–791 (2008).
8. W. Shi, Y. Tian, and A. Gervais, "Scaling capacity of fiber-optic transmission systems via silicon photonics," Nanophotonics **9**(16), 4629–4663 (2020).
9. J. L. Pita Ruiz, L. G. Rocha, and J. Yang, *et al.*, "Ultracompact silicon-on-insulator couplers for multicore fibers," ACS Photonics **10**(4), 953–958 (2022).
10. J. L. P. Ruiz, L. G. Rocha, and J. Yang, *et al.*, "Efficient integrated tri-modal coupler for few-mode fibers," Opt. Express **30**(2), 2539–2546 (2022).
11. J. L. P. Ruiz, L. G. Rocha, and J. Yang, *et al.*, "Compact dual-polarization silicon integrated couplers for multicore fibers," Opt. Lett. **46**(15), 3649–3652 (2021).
12. X. S. Yao, H. Xuan, and X. Chen, *et al.*, "Polarimetry fiber optic gyroscope," Opt. Express **27**(14), 19984–19995 (2019).
13. J. Wang and Y. Long, "On-chip silicon photonic signaling and processing: a review," Sci. Bull. **63**(19), 1267–1310 (2018).
14. S. Guerber, C. Alonso-Ramos, and D. Benedikovic, *et al.*, "Broadband polarization beam splitter on a silicon nitride platform for o-band operation," IEEE Photonics Technol. Lett. **30**(19), 1679–1682 (2018).
15. R. Kudalippalliyalil, T. E. Murphy, and K. E. Grutter, "Low-loss and ultra-broadband silicon nitride angled mmi polarization splitter/combiner," Opt. Express **28**(23), 34111–34122 (2020).
16. X. Sun, J. S. Aitchison, and M. Mojahedi, "Realization of an ultra-compact polarization beam splitter using asymmetric mmi based on silicon nitride/silicon-on-insulator platform," Opt. Express **25**(7), 8296–8305 (2017).
17. K. Gallacher, P. F. Griffin, and E. Riis, *et al.*, "Silicon nitride waveguide polarization rotator and polarization beam splitter for chip-scale atomic systems," APL Photonics **7**(4), 046101 (2022).
18. M. A. Barrow, T. E. Murphy, and K. E. Grutter, "Broadband, fabrication-tolerant polarization rotators in silicon nitride," in *2023 IEEE Silicon Photonics Conference (SiPhotonics)*, (IEEE, 2023), pp. 1–2.
19. Y. R. Bustamante, R. A. de Paula, and I. Aldaya, "Inverse design of a broadband silicon nitride polarization rotor," in *Frontiers in Optics*, (Optical Society of America, 2021), pp. JW7A–91.
20. C. Yin, Y. Zhou, and W. Zhang, *et al.*, "All-silicon and ultra-compact transverse electric-pass polarizer with large bandwidth and high polarization extinction ratio based on subwavelength metamaterials," Opt. Eng. **61**(11), 117103 (2022).
21. Y. Chen, J. Zhang, and M. Zhu, *et al.*, "Ultra-compact and broadband all-silicon tm-pass power splitter using subwavelength holey-structured metamaterial waveguides," Opt. Express **30**(25), 44604–44616 (2022).
22. S. Wu, J. Hao, and Z. Zhao, *et al.*, "Low loss and high extinction ratio all-silicon tm-pass polarizer with reflection removal enabled by contra-mode conversion bragg-gratings," Opt. Express **29**(17), 27640–27652 (2021).
23. M. Barona-Ruiz, C. Pérez-Armenta, and A. Ortega-Mo nux, *et al.*, "Broadband and low-loss tm-pass polarizer using tilted subwavelength structures," Opt. Express **30**(21), 38930–38937 (2022).
24. Y. Dong, Y. Liu, and Y. Xu, *et al.*, "On-chip design of a broadband 850 nm tm-pass/te-stop polarizer with tilted subwavelength gratings," Symmetry **14**(11), 2359 (2022).
25. C. Xiang, W. Jin, and J. E. Bowers, "Silicon nitride passive and active photonic integrated circuits: Trends and prospects," Photonics Res. **10**(6), A82–A96 (2022).
26. P. Xu, Y. Lu, and Z. Yu, *et al.*, "Ultra-compact active te and tm pass polarizers based on ge_2 sb_2 te_5 in silicon waveguide," IEEE Photonics Technol. Lett. **28**(23), 2697–2700 (2016).
27. X. Hu and J. Wang, "Ultrabroadband compact graphene–silicon tm-pass polarizer," IEEE Photonics J. **9**(2), 1–10 (2017).
28. B. Bai, L. Liu, and R. Chen, *et al.*, "Low loss, compact tm-pass polarizer based on hybrid plasmonic grating," IEEE Photonics Technol. Lett. **29**(7), 607–610 (2017).
29. R. Chen, B. Bai, and Z. Zhou, "Low-loss hybrid plasmonic tm-pass polarizer using polarization-dependent mode conversion," Photonics Res. **8**(7), 1197–1202 (2020).
30. M. G. Saber, N. Abadía, and D. V. Plant, "Cmos compatible all-silicon tm pass polarizer based on highly doped silicon waveguide," Opt. Express **26**(16), 20878–20887 (2018).
31. S. Wu, Z. Guo, and T. Feng, *et al.*, "Compact and ultra-broadband all-silicon tm-pass and te-reflected polarizer using grating based weakly coupled nanowires," Opt. Express **30**(17), 29844–29855 (2022).

Optics EXPRESS

32. X. Guan, P. Chen, and S. Chen, *et al.*, "Low-loss ultracompact transverse-magnetic-pass polarizer with a silicon subwavelength grating waveguide," Opt. Lett. **39**(15), 4514–4517 (2014).
33. J. M. Luque-González, A. Sánchez-Postigo, and A. Hadij-ElHouati, *et al.*, "A review of silicon subwavelength gratings: building break-through devices with anisotropic metamaterials," Nanophotonics **10**(11), 2765–2797 (2021).
34. K. J. Lee, J. Giese, and L. Ajayi, *et al.*, "Resonant grating polarizers made with silicon nitride, titanium dioxide, and silicon: design, fabrication, and characterization," Opt. Express **22**(8), 9271–9281 (2014).